How processing of aspartylphosphate is coupled to lumenal gating of the ion pathway in the calcium pump

Chikashi Toyoshima*, Yoshiyuki Norimatsu, Shiho Iwasawa, Takeo Tsuda, and Haruo Ogawa

Institute of Molecular and Cellular Biosciences, University of Tokyo, 1-1-1 Yayoi, Bunkyo-ku, Tokyo 113-0032, Japan

Contributed by Chikashi Toyoshima, October 19, 2007 (sent for review October 5, 2007)

Ca^{2+}-ATPase of skeletal muscle sarcoplasmic reticulum is the best-studied member of the P-type or E1/E2 type ion transporting ATPases. It has been crystallized in seven different states that cover nearly the entire reaction cycle. Here we describe the structure of this ATPase complexed with phosphate analogs BeF_3^- and AlF_4^- in the absence of Ca^{2+}, which correspond to the E2P ground state and E2~P transition state, respectively. The luminal gate is open with BeF_3^- and closed with AlF_4^-. These and the E1~P·ADP analog crystal structures show that a two-step rotation of the cytoplasmic A-domain opens and closes the luminal gate through the movements of the M1–M4 transmembrane helices. There are several conformational switches coupled to the rotation, and the one in the cytoplasmic part of M2 has critical importance. In the second step of rotation, positioning of one water molecule couples the hydrolysis of aspartylphosphate to closing of the gate.

crystal structure | phosphorylation | P-type ATPase

Ca^{2+}-ATPase from skeletal muscle sarcoplasmic reticulum (SERCA1a) is an ATP-powered calcium pump that transfers Ca^{2+} from the cytoplasm to the lumen of sarcoplasmic reticulum against a $>10^4$ concentration gradient. It is an integral membrane protein of M_r 110K (1), and it pumps ions by alternating the affinity of the transmembrane (TM) binding sites and synchronizing opening and closing of the cytoplasmic and luminal gates. According to the conventional E1–E2 theory (2–4), E1 and E2 respectively refer to high-affinity and low-affinity states to Ca^{2+}. Gating of the ion pathway is coupled to autophosphorylation and dephosphorylation of the ATPase. Phosphoryl transfer from ATP to an Asp in the cytoplasmic domain (i.e., $E1{\cdot}2Ca^{2+} \rightarrow E1P$; here P stands for phosphorylated state) closes the cytoplasmic gate, and the release of ADP triggers a change in affinity of the Ca^{2+} binding sites (i.e., $E1P \rightarrow E2P$) and opening of the luminal gate. Hydrolysis of the aspartylphosphate ($E2P \rightarrow E2$) closes the gate.

X-ray crystallography of SERCA1a has established that the ATPase consists of three cytoplasmic domains (A, actuator; P, phosphorylation; and N, nucleotide binding) and 10 TM (M1–M10) helices (5). Crystal structures have been determined for seven different states [$E1{\cdot}2Ca^{2+}$, E1·AMPPCP, $E1{\cdot}AlF_x{\cdot}$ADP, $E2{\cdot}AlF_4^-$(TG), $E2{\cdot}MgF_4^{2-}$(TG), E2(TG), and E2·AMPPCP(TG)] (5–11) that cover nearly the entire reaction cycle by fixing the structure with appropriate ligands or their analogs. These structures demonstrate that the ATPase undergoes very large domain movements during the reaction cycle (12). AlF_4^- and MgF_4^{2-}, respectively, have been used for transition state and product state analogs of phosphate, partly describing the $E2P \rightarrow E2$ dephosphorylation reaction. Yet the structure for the ground state analog $E2{\cdot}BeF_x$ is indispensable because only with this complex is the luminal gate open and the Ca^{2+} binding sites accessible from the luminal side (13, 14).

The structure of the E2P ground state is expected to be significantly different from the $E2{\cdot}AlF_4^-$ transition state analog: The subtle changes that normally occur between ground and transition states of most enzymes will be too small for directly moving helices for gating at ≈50 Å away. 2′,3′-*O*-(2,4,6-trinitrophenyl)adenosine 5′-monophosphate (TNP-AMP) superfluorescence, an indicator of the E2P ground state in the cytoplasmic domains, and intrinsic tryptophan fluorescence, mostly reporting on movements in the TM helices, also suggest rather large differences between the $E2{\cdot}BeF_x$ and $E2{\cdot}AlF_4^-$ (13).

So far, all successful crystallization of SERCA in the absence of Ca^{2+} used potent inhibitors like thapsigargin (TG) (6, 8, 10) or α-cyclopiazonic acid (15, 16) to stabilize the inherently unstable TM domain. TG does not seem to cause much perturbation of $E2{\cdot}MgF_4^{2-}$ and $E2{\cdot}AlF_4^-$ because their TM structures are already E2-like (13, 17). In the case of $E2{\cdot}BeF_x$, although the inhibitors alter the arrangement of TM helices and close the luminal gate, flexible links between the cytoplasmic and TM domains (16) keep the cytoplasmic domains from being affected by inhibitors (13). In fact, superfluorescence from TNP-AMP remains the same level even after binding of TG (13).

Therefore, crystallization of the ATPase in $E2{\cdot}BeF_x$ was attempted in the presence and absence of TG and yielded crystals that diffracted to 2.4-Å (+TG) and 3.8-Å (−TG) resolution. At 2.4-Å resolution, it was evident that the bound BeF_x is BeF_3^-, demonstrating that the structure is a good mimic of the ground state. The structure of $E2{\cdot}BeF_3^-$(−TG), although details are of course limited, clearly showed the movements of domains and helices [supporting information (SI) Fig. 8]. Furthermore, the structure turned out to be a combination of parts visualized at high resolution in other states, placing confidence in the accuracy.

We also improved the resolution of the crystal structures of $E1{\cdot}AlF_x{\cdot}$ADP (8, 9) and $E2{\cdot}AlF_4^-$(TG) (10) and show that the bound species is AlF_4^- in either crystal, indeed indicating a transition state-like complex. Thus, we can now describe a $E1P \rightarrow E2P \rightarrow E2{\cdot}Pi$ reaction in some detail including water molecules. These four structures are substantially different and reveal how the processing of the aspartylphosphate is coupled to opening and closing of the luminal gate.

Results

Crystallization and Structure Determination. Crystals were made by the dialysis method in the presence of exogenous phospholipid (phosphatidylcholine). Structures were solved by molecular replacement starting from the atomic model for $E2{\cdot}MgF_4^{2-}$ [Protein Data Bank (PDB) ID code 1WPG] (8) and refined to an

Author contributions: C.T. designed research; C.T., S.I., and T.T. performed research; C.T., Y.N., and H.O. analyzed data; and C.T. wrote the paper.

The authors declare no conflict of interest.

Data deposition: The atomic coordinates for $E1{\cdot}AlF_4^-$·ADP, $E2{\cdot}BeF_3^-$(−TG), $E2{\cdot}BeF_3^-$(TG), and $E2{\cdot}AlF_4^-$(TG) forms of Ca^{2+}-ATPase have been deposited in the Protein Data Bank, www.pdb.org (PDB ID codes 2ZBD, 2ZBE, 2ZBF and 2ZBG, respectively).

*To whom correspondence should be addressed. E-mail: ct@iam.u-tokyo.ac.jp.

This article contains supporting information online at www.pnas.org/cgi/content/full/0709978104/DC1.

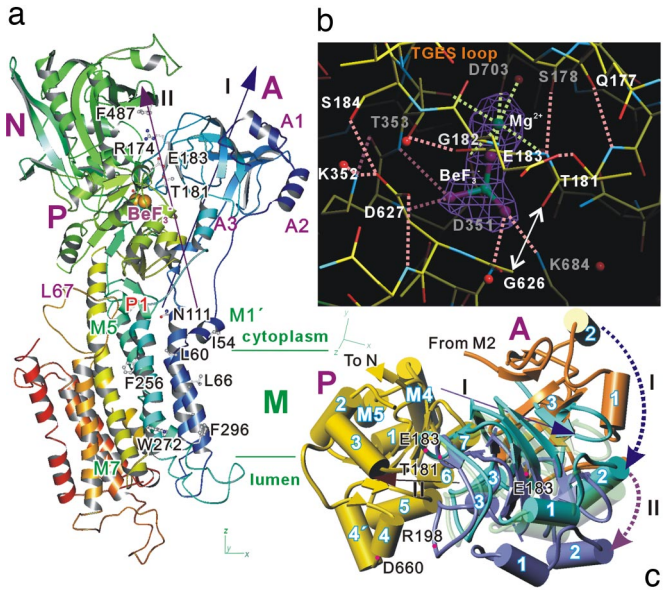

Fig. 1. Structure of the BeF_3^- complex of Ca^{2+}-ATPase in the absence of Ca^{2+} and a comparison of the cytoplasmic domains with other phosphorylated intermediate analogs. (*a*) Ribbon model of E2·BeF_3^-(−TG), with several marker residues in ball and stick. The image was prepared with Molscript (33). (*b*) Details around the phosphorylation site in E2·BeF_3^-(TG). (*c*) Positions of the A-domain relative to the P-domain in E1·AlF_4^-·ADP (orange), E2·BeF_3^-(−TG) (light green), E2·BeF_3^-(TG) (cyan, transparent), and E2·AlF_4^-(TG) (blue gray). The P-domain is shown only for E2·BeF_3^-(TG). The purple net in *b* represents an $|F_o| - |F_c|$ electron density map contoured at 6σ at 2.4-Å resolution before introducing BeF_3^- and Mg^{2+} into the atomic model. Rotation axes for E1·AlF_4^-·ADP → E2·BeF_3^-(−TG) (I) and E2·BeF_3^-(−TG) → E2·AlF_4^-(TG) (II) are specified in *a* and *c*. In *b*, pink broken lines show likely hydrogen bonds and the white arrow a van der Waals contact.

R_{free} of 25.8% at 2.4-Å resolution for E2·BeF_3^-(TG). Crystals grown in the absence of TG [E2·BeF_3^-(−TG)] diffracted to 3.8-Å resolution. The unit cell parameters were very similar to E2·BeF_3^-(TG) before dehydration (see *Methods*), and molecular replacement was straightforward. At 2.4-Å resolution, it was evident that the bound phosphate analog is BeF_3^-, as an $|F_o| - |F_c|$ electron density map showed clear triangular density above the phosphorylated residue Asp-351 (Fig. 1*b*) . The distance between the Be and the carboxyl oxygen (1.60 Å), obtained by refinement using CNS (18) assuming zero radius for Be, was very similar to that observed with the BeF_3^- complex of phosphoserine phosphatase (1.58 Å) (19). Therefore, as demonstrated by biochemical studies (13, 14), BeF_3^- forms an E2P ground state analog, although TG was included for crystallization.

E2·AlF_4^-(TG) crystals in two different space groups (i.e., *C*2 and $P2_12_12$) diffracted to 2.6-Å resolution and yielded virtually identical structures, similar to that reported previously (10) considering the difference in resolution (2.6 Å vs. 3.0 Å). The atomic models also were identical to that of E2·MgF_4^{2-}(TG), a product state analog, determined at 2.3-Å resolution (8), except for details around the phosphorylation site. At 2.6-Å resolution, it was unambiguous that AlF_4^-, not AlF_3, is bound, confirming the earlier biochemical assignment (20). The distance between the Al and Asp-351 carboxyl and the distance between the Al and attacking water were 1.98 Å. The crystals of E1·AlF_x·ADP also were improved and yielded a 2.4-Å resolution structure, which showed that, here also, the bound AlF_x is AlF_4^-, different from our previous model (PDP ID code 1WPE) (8). A ribbon model for E2·BeF_3^-(−TG) is presented in Fig. 1*a*, and its superimposition with E2·AlF_4^-(TG) is presented in Fig. 2*b*.

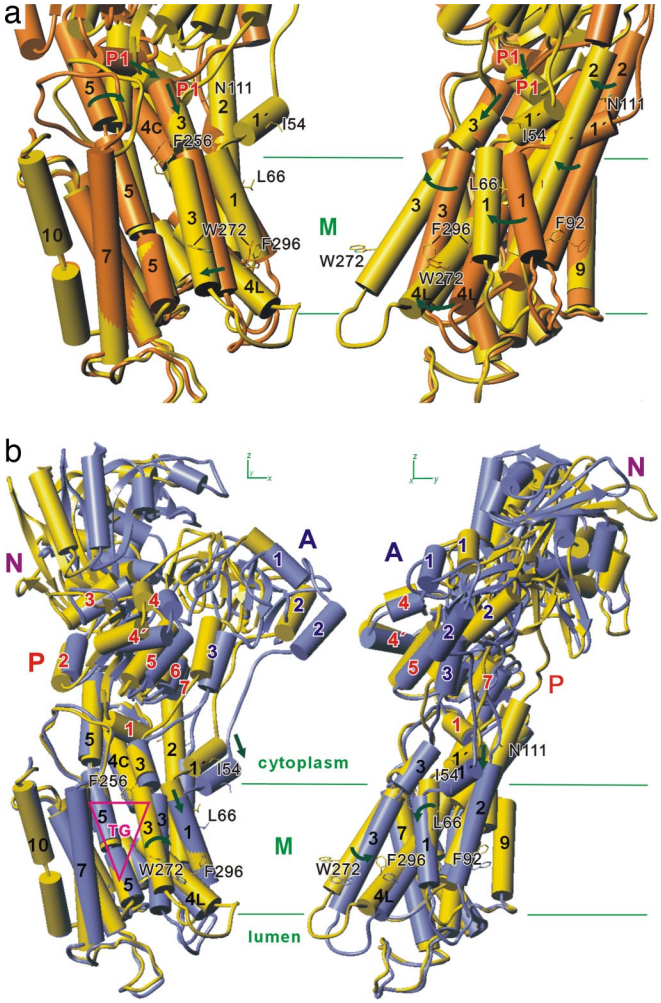

Fig. 2. Superimposition of the models for phosphorylated intermediate analogs fitted with the M7–M10 helices. Helices are represented with cylinders with marker residues in stick. The colors used are yellow, E2·BeF_3^-(−TG); orange, E1·AlF_4^-·ADP; and blue gray, E2·AlF_4^-(TG). Small arrows show movements in the transition from E1P → E2P (*a*) and E2P → E2~P (*b*). The TG binding site is indicated with an inverted triangle (*b*).

Differences in Domain Arrangement Between E2·BeF_3^- and E2·AlF_4^-(TG). Overall domain arrangement in E2·BeF_3^- is similar to that in E2·AlF_4^-(TG) (10) and E2·MgF_4^{2-}(TG) (8); that is, the cytoplasmic domains form a compact headpiece in which the A-domain is nearly 90° rotated from the E1~P·ADP analog around an axis approximately perpendicular to the membrane (Fig. 1 *a* and *c*). Nevertheless, the cytoplasmic headpiece in E2·BeF_3^- is more upright (≈10° for the P-domain and ≈20° for the N-domain) (Fig. 2*b*), because the A-domain is wedged deeper into the P–N interface, and the A-domain less rotated (by 25° with respect to the P-domain) (Fig. 1*c*). E2·BeF_3^-(TG) is intermediate between them (Fig. 1*c*). The more upright N-domain and the less rotated A-domain suggest that the rotations accompanying the E1P → E2P ground state and that for E2P → E2·Pi are of a different nature, because the interface between the N- and A-domains in E2·BeF_3^- is the same as those in E2·AlF_4^-(TG) and E2·MgF_4^{2-}(TG). We can identify only one hydrogen bond (Ser-186–Glu-439) other than that between Thr-171 and Glu-486, observed in both E1·AMPPCP and E2·MgF_4^{2-}(TG) (8).

The axis of rotation was identified with Dyndom (21). For the transition between E1·AlF_4^-·ADP and E2·BeF_3^-, the axis of

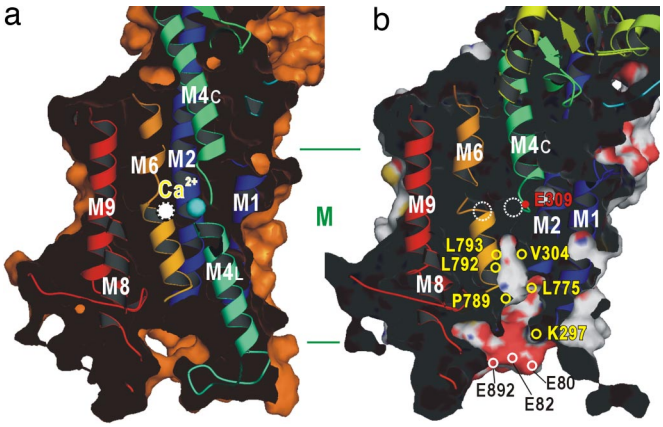

Fig. 3. Cross-sections of the transmembrane region of Ca^{2+}-ATPase. van der Waals surfaces of E1·AlF_4^-·ADP (*a*) and E2·BeF_3^-(−TG) (*b*). Red colors represent acidic residues. Dotted circles in *b* indicate the positions of Ca^{2+} observed in E1·AlF_4^-·ADP (*a*). The images shown were prepared with PyMol (34).

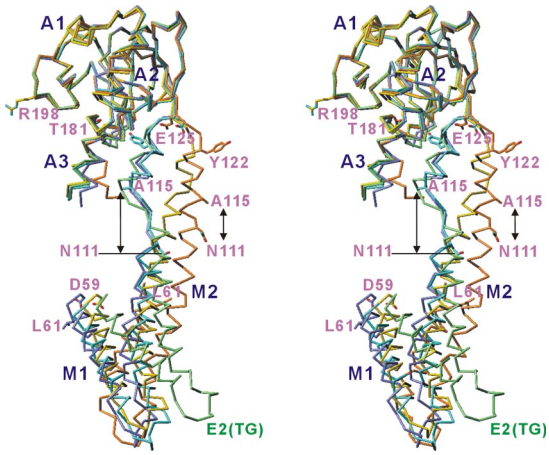

Fig. 4. Atomic models fitted with the A-domain, illustrating the M2 switch. C^{α} traces of the A-domain and the M1–M2 helices (Asp-59–Thr-242) are shown in stereo with side chains of several marker residues. The colors used are orange, E1·AlF_4^-·ADP; yellow, E2·BeF_3^-(−TG); cyan, E2·BeF_3^-(TG); blue gray, E2·AlF_4^-(TG); and lime, E2(TG+BHQ) (also marked). Arrows represent the distances between Asn-111 and Ala-115 in E1·AlF_4^-·ADP and E2·AlF_4^-(TG).

rotation runs through the M2 side of Ala-725 (on the P7 helix), ≈25° inclined from the membrane normal toward $+x$ (Fig. 1 *a* and *c*). The axis for rotation between E2·BeF_3^- and E2·AlF_4^-(TG) runs near Thr-181 and Pro-709 (on P6) and is inclined by −20° (Fig. 1 *a* and *c*). The two axes are ≈17 Å distant. Therefore, the structural changes accompanying E1P → E2·Pi occur in two distinct steps.

First Step Rotation: Opening of the Luminal Gate. By comparing E1·AlF_4^-·ADP and E2·MgF_4^{2-}(TG) crystal structures, we previously postulated that opening of the luminal gate is realized by a downward movement of the M4 helix and tilting away from M5 of the luminal half of M4 (M4L) (8). These movements are generated by rotation of the A-domain, which moves the V-shaped structure formed by the M1 and M2 helices and thereby M4 through van der Waals contacts between M1 and M4L. Corroborating this earlier expectation, we now see in E2·BeF_3^-(−TG) that the M3 and M4 helices have moved downward and swayed toward M3 (i.e., $-y$ direction), making a large empty space surrounded by M1, M2, M4, and M6. As a result, the luminal gate is opened (Figs. 2*a* and 3). The hole is lined by hydrophobic residues just below Ca^{2+}-binding site II and by negatively charged residues near the luminal end (Fig. 3).

In addition to the M1–M4 contacts, one end of the V-shape (around Leu-60 on M1) (Fig. 1*a*) makes van der Waals contacts with the M3 helix, providing either a means for pushing M3 when it has a room for movement or a pivot for the rotation/tilting of the V-shaped structure. In the first step, the V-shaped structure does not change its axial height, but pushes M3 toward M7 at Leu-60 and Leu-61 (M1) and Gly-257 (M3). The top of M3 is pushed down by the P1 helix in the P-domain (Fig. 2*a*), in particular, by Pro-337, which makes contacts with Pro-248 at the top of M3 in E1·AlF_4^-·ADP and travels >10 Å during the transition to E2·BeF_3^- and stays there. The structure around Pro-248 (SI Fig. 8) appears identical through E2P to E2 and provides, together with the loop connecting M6 and M7 (L67 in Fig. 1*a*), the pivot for step 2 movements. This loop also assumes two structures: one from E1·2Ca^{2+} to E1·AlF_4^-·ADP (type E1) and the other from E2·BeF_3^-(−TG) to E2(TG) (type E2). Thus the M3 helix sways in the $-y$ direction through a downward push from P1 and a sideways push at the middle from M1.

The M4 helix is integrated into the P-domain. Therefore, by the bowing of M5 and, accordingly, by the inclination of the P-domain, M4 is pushed downwards and tilts in the $-y$ direction guided by other helices, in particular M1 and M2. A closed position of M4 is prevented by Leu-75 on M1, because superimposition of M1 in E2·BeF_3^-(−TG) and M4 in E2·AlF_4^-(TG) shows a collision at Leu-75-V300 (SI Fig. 9*b*). Superimposition of the M_3^-M4 helices in various states show that they do not move as a rigid body. Leu-65, which blocks the conformational changes of the Glu-309 side chain to realize the occluded state in E1·AMPPCP and E1·AlF_4^-·ADP (7), is still in position; Ile-97 (M2) and Leu-797 (M6) may also contribute to keep the cytoplasmic gate closed (SI Fig. 9*a*).

Second Step Rotation: Closing of the Luminal Gate and Hydrolysis of Aspartylphosphate. The next step, the transition from the E2P ground state to the E2·Pi product state, is realized by a further rotation (by 25°) of the A-domain but around a different axis (Figs. 1 *a* and *c*). Conspicuous movements here are a downward displacement of the M1–M2 V-shaped structure and a tilting of the M3–M4 helices to close the luminal gate. Because superimposition of M1 in E2·AlF_4^-(TG) and M4 in E2·BeF_3^-(−TG) produces collisions at Leu-65 (M1)–Val-304 (M4) and Ala-68 (M1)–Val-300 (M4), the latter movement is likely to be caused by a push from M1 on M4L (SI Fig. 9*b*). Another push could come through M3, because Ile-264, Ile-267, and Cys-268 are in van der Waals contacts with residues on M4; Ile-260 (M3) is indeed in contact with Leu-61 (M1). Then the question is what drives the V-shaped structure toward the lumen. It was most convenient to compare E2·BeF_3^-(±TG) (SI Fig. 10) to address this question.

A Switch in the M2 Helix. In E2·BeF_3^-(TG), the azimuthal position of the A-domain is very close to that in E2·BeF_3^-(−TG) (different by ≈6°) (Fig. 1*c*), yet the V-shaped structure is positioned ≈6 Å lower (SI Fig. 10) and the relative disposition of the TM helices is virtually the same as that in E2·AlF_4^-(TG) (Fig. 2*b*). Evidently, the movement of the V-shaped structure is related to an unwinding of the top (cytoplasmic) part of the M2 helix (Fig. 4). From E1·2Ca^{2+} to E1·AlF_4^-·ADP, i.e., in the E1 states, M2 is a continuous helix from the luminal end to near the A-domain (Ile-85–Tyr-122); in contrast, in E2·BeF_3^-(TG), E2·AlF_4^-(TG), E2·MgF_4^{2-}(TG), and E2(TG), that is, in the E2 states, the part between Asn-111–Ala-115 is unwound, leaving a short helical segment (Ala-115–Tyr-122) at the cytoplasmic end. The unwinding increases the distance between Asn-111 and Ala-115 by ≈7 Å and allows the M2 helix to take different paths (Fig. 4). The junction between the

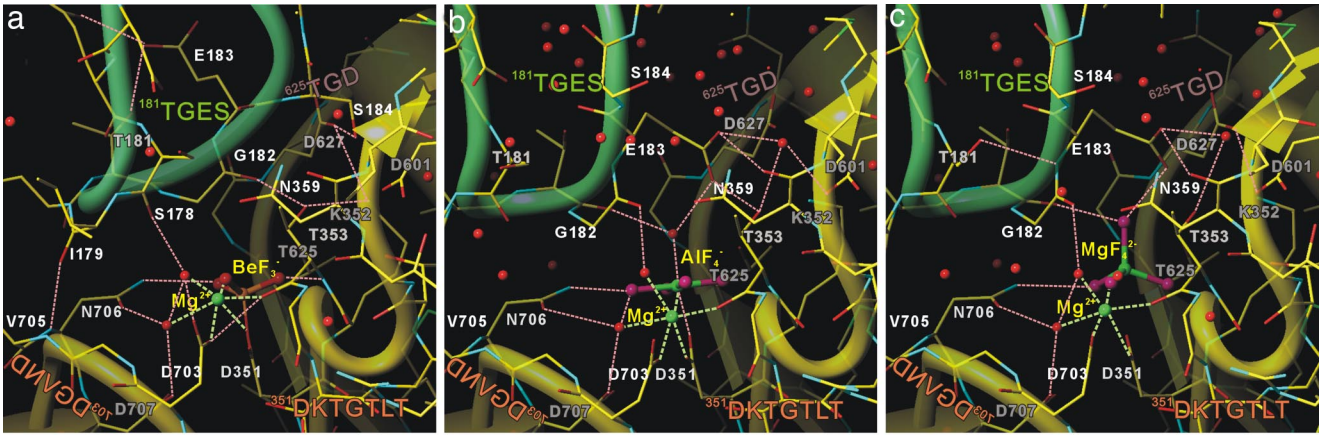

Fig. 5. Details of the phosphorylation site in the phosphorylated intermediate analogs. (*a*) E2·BeF_3^-(TG), E2P ground state analog. (*b*) E2·AlF_4^-(TG), E2~P transition state analog. (*c*) E2·MgF_4^{2-}(TG) (PDB ID code 1WPG), E2·Pi product state analog. Broken lines in pink show likely hydrogen bonds, and those in light green show Mg^{2+} coordination. Small red spheres represent water molecules. The conserved sequence motifs are shown.

β-strand Aβ1 and M2 contains Glu-125, the dihedral angle of which is 180° different between the two states. Thus, Glu-125 is a kind of swivel. This M2 switch is on the E1 side in E2·BeF_3^-(−TG) and the E2 side in E2·BeF_3^-(TG), and it determines the axial position of the V-shaped structure (Fig. 4).

What kind of force unwinds M2 is unclear in the case of E2·BeF_3^-(TG). However, in the transition from E2P to E2·Pi, a further rotation of the A-domain must be the cause. Such a rotation will bend the upper part of the M2 helix and cause unwinding because the TM part of the V-shaped structure, which is already pressed against the M3 helix, cannot move further.

Structure of the Phosphorylation Site. Then how is the second-step rotation related to the hydrolysis of the aspartylphosphate? We previously described the crystal structure of E2·MgF_4^{2-}(TG), a product state analog of dephosphorylation, at 2.3-Å resolution (Fig. 5*c*) (8). In this state, the phosphate analog MgF_4^{2-} was located above Asp-351 carboxyl at a 2.5-Å distance, and the fluorine at the top of the tetrahedron was located at a hydrogen bond distance from the Glu-183 carboxyl in the signature sequence ^{181}TGES of the A-domain (Fig. 5*c*). In addition, by superimposing an aspartylphosphate taken from Spo0A (22), a member of the related response regulator family, we proposed that a water molecule would replace the fluorine at the top of the tetrahedron for in-line attack on the aspartylphosphate, activated by Glu-183 (8). Mutagenesis studies (23–26) support this idea.

In E2·BeF_3^-(TG), Gly-182, which contributes in E2·MgF_4^{2-}(TG) to the coordination of the Mg^{2+} bound to Asp-703 through a water molecule (Fig. 5*c*), occupies the space immediately above the BeF_3^- (Fig. 5*a*). Gly-182$^{\alpha}$ makes van der Waals contacts with the Be and all three F atoms in BeF_3^-, thereby blocking water access to BeF_3^-, as demonstrated by van der Waals surface of the atomic model with explicit hydrogens (Fig. 6). This position of Gly-182 is stabilized by a hydrogen bond between Gly-182 carbonyl and Thr-353 hydroxyl (Figs. 1*b* and 5*a*). Instead of Gly-182, Ser-186 carbonyl coordinates Mg^{2+} through a water molecule in E2·BeF_3^-(TG).

In contrast, in E2·AlF_4^-(TG), the TGES loop is retracted from the phosphorylation site and makes a space for accommodating only one water molecule immediately above AlF_4^- (Figs. 5*b* and 6*b*). This water molecule appears to have an ideal hydrogen-bonding geometry with Glu-183 carboxyl and Gly-182 carbonyl. If the hydrogen is withdrawn by the Glu-183 carboxyl, the water molecule becomes activated and will make an in-line attack on the aspartylphosphate. Confirming the earlier expectation (8), this water molecule in E2·AlF_4^-(TG) occupies the same position as the F atom at the top of MgF_4^{2-} in E2·MgF_4^{2-}(TG). The positions of the coordinating side chains also are identical to those in the product state analog, although AlF_4^- does not form a proper pentacoordinated transition state analog. Thus, the three crystal structures shown in Fig. 5 provide a fair description of the reaction intermediates.

Switching Between the First and Second Steps of Rotation: The Role of the TGES Loop. The rotation in the first step is terminated by deep insertion of the TGES loop into the phosphorylation site. The Ser-184 side chain forms a hydrogen bond with Asp-627, an absolutely conserved residue in P-type ATPases, located on the opposite side of the phosphorylation residue Asp-351 (Figs. 1*b* and 5*a*). Gly-182 carbonyl comes within a hydrogen bond distance of the Thr-353 hydroxyl, and, perhaps more importantly, the Thr-181 carbonyl makes van der Waals contact with Gly-626 C$^{\alpha}$ (Fig. 1*b*), another absolutely conserved residue in the ^{625}TGD motif, thereby making a new pivoting point for the second step rotation (Fig. 1*c*).

The positioning of the A-domain in the E2P ground state appears to be done solely through the TGES loop. In E2·BeF_3^-(TG), we see many unique hydrogen bonds that locate

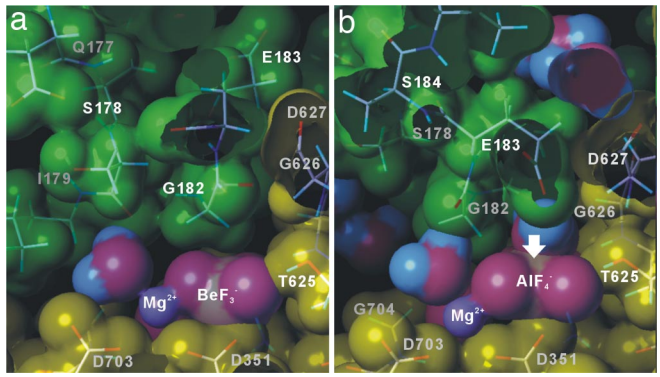

Fig. 6. Surface representation of the atomic models for the phosphorylation site in the E2P and E2~P analogs. The van der Waals surface is superimposed on the atomic model of E2·BeF_3^-(TG) (*a*) or E2·AlF_4^-(TG) (*b*) with explicit hydrogens. Green spheres represent the atoms in the A-domain; yellow spheres represent those in the P-domain. Phosphate analogs (dimensions taken from phosphate), Mg^{2+} (blue violet spheres), and water (red and cyan spheres) are shown in atom colors. The white arrow in *b* indicates the attacking water molecule. Thr-353 is located on the front side and not seen here.

the TGES loop precisely with respect to the P-domain (Fig. 5*a*): The one between the Ile-179 and Val-705 main chains may be of particular importance, because the two domains nicely engage here near the pivoting point. In contrast, an electrostatic catch between the P6 and A3 helices observed in E2·MgF_4^{2-}(TG) (8) is incomplete in E2·BeF_3^-(TG) and may not be formed at all in E2·BeF_3^-(−TG) (Fig. 1*c*).

In the second step, the A-domain rotates further (≈25°) but now around an axis near Thr-181 (II in Fig. 1 *a* and *c*). The TGES loop retracts from the phosphorylation site, forming a space just sufficient for accommodating the attacking water molecule. Here again, accurate positioning of the TGES loop is important. In addition to the electrostatic catch, we noticed that a cluster of hydrophobic residues is formed around Tyr-122 (27) by the changing of the M2 switch, restricting the rotation of Ile-179. In addition, near the pivot of rotation, the Leu-180 carbonyl makes contacts with Pro-681. These hydrophobic contacts appear to restrict the conformational change of the TGES loop. Thus, different parts of the A-domain are used for terminating its two successive rotations.

In the crystal structures of SERCA1a in seven different states, the variation within structure of the A-domain itself is limited to the TGES loop (Ser-178–Ser-186) (Fig. 4), delimited by main chain hydrogen bonds between Val-175–Val-187 and Asp-176–Asn-213. The conformation of the TGES loop in E2·BeF_3^-(TG) is identical to that in E1·AlF_4^-·ADP but significantly different from that in E2·AlF_4^-(TG) or E2·MgF_4^{2-}(TG). Thus, here again, we see E1- and E2-type switches. In E2·BeF_3^-(TG), the Glu-183 carboxyl forms a hydrogen bond with Thr-181 and is accommodated inside of the TGES loop (Fig. 5*a*), as in E1·AlF_4^-·ADP. This hydrogen bond may be responsible for fixing the TGES loop in a specific shape. Flipping in of the Glu-183 side chain into the phosphorylation site is prevented by the Asp-627 side chain, which is firmly stabilized by the Lys-352 and Ser-184 side chains (Figs. 1*b* and 5*a*). Thus, for a water molecule to come above the aspartylphosphate, retraction of the TGES loop will be a prerequisite. Presumably, to facilitate this retraction, the bottom of the TGES loop is flat and the Asn-706 side chain forms a flat platform on the P-domain side. Mg^{2+} might be used to precisely define the distances, because the Gly-182 (E2·AlF_4^-(TG) and E2·MgF_4^{2-}(TG)) or Ser-178 carbonyl (E2·BeF_3^-(TG)) coordinates the Mg^{2+} through a water molecule (Fig. 5).

Discussion

We describe here how Ca^{2+}-ATPase couples the processing of phosphorylated aspartate to luminal gating of the ion pathway based on four crystal structures that represent the E1∼P·ADP, E2P, E2∼P, and E2·Pi states. Consistent with earlier biochemical studies (13, 14), only E2·BeF_3^-(−TG), which represents the E2P ground state, exhibits an opened ion pathway to the lumen of sarcoplasmic reticulum. Confirming our earlier proposal (8), the gating is achieved by changing the orientation of M4L through the V-shaped structure formed by M1 and M2, coupled to a two-step rotation of the A-domain. The TGES loop in the A-domain regulates the positioning of the attacking water molecule, thereby coupling the chemical reaction and gating. During the transition from E1P to E2P, the phosphoryl group itself moves only 1 Å (see also the animation in SI Movie 1).

A Two-Step Rotation for the Gating of the Ion Pathway. The mechanism of the luminal gating is illustrated in Fig. 7. In the E1P → E2P transition, the A-domain rotates 90° around an axis ≈25° inclined from the membrane normal, bringing the TGES loop deep into the P-domain above the aspartylphosphate. This rotation seems to arise mostly from strain imposed on the -domain–M3 link in E1P (8, 28) and causes inclination of the A- and the P-domains toward M1. This inclindation arises because the upper surface of the P-domain, on which the A-domain sits,

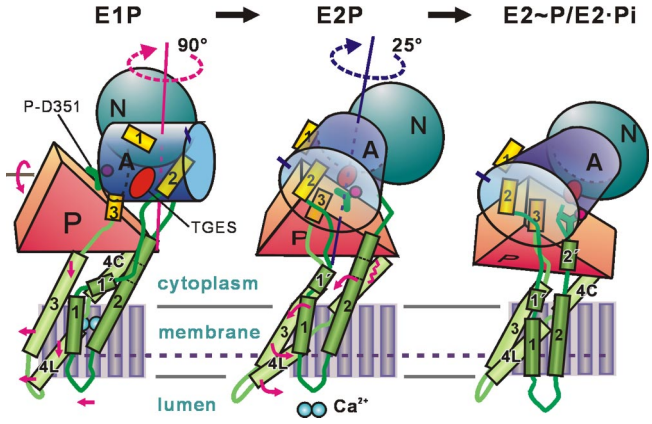

Fig. 7. A cartoon illustrating two-step rotation in the processing of aspartylphosphate and gating of the ion pathway. Small arrows indicate the movements of the TM helices. The M1–M4 (green) and A1–A3 (yellow) helices are numbered. P-D351 refers to phosphorylated Asp-351.

is inclined with the M3 side higher up. As the rotation proceeds, the distal end of the A-domain, that is, the end connected to the M1′ helix, would be raised if it were not anchored in the membrane. However, although flexible, the length of the A-domain–M1′ loop cannot change much. Due to this restraint, the A-domain and, accordingly, the P-domain have to incline toward M1, pushing down the M3 and M4 helices to the E2 position. At the same time, the V-shaped structure composed of M1 and M2 follows the rotation of the A-domain and pushes M3 and M4L sideways. As a result, the luminal gate is opened and Ca^{2+} is released.

The second rotation of 25° of the A-domain occurs around an axis formed by the first rotation, near Thr-181. This step corresponds to the E2P → E2·Pi transition. The second rotation is allowed only after retraction of the TGES loop from its deep position in the phosphorylation site and stops when the attacking water is introduced and fixed by the TGES loop. This further rotation causes an unwinding of a cytoplasmic part of M2 and changes its path toward M1; the V-shaped structure inclines, pivoting on M3, and moves downward as the distal end of the A-domain moves farther down (≈5 Å). This downward movement of the V-shaped structure presses on M3 and M4 to close the gate. Finally, the phosphate is released from the phosphorylation site and closing of the gate is ensured.

The E2P ground state is realized in the end of the first rotation, and a number of hydrogen bonds are formed only in this state between the TGES loop and the P-domain. Kinetically this makes sense, because it allows sufficient time for the transition into and out of E2P for releasing Ca^{2+} into the lumen. Mutagenesis studies on Thr-181 and Ser-184 highlighted their importance in the E1P → E2P transition (25, 26), nicely consistent with the structural roles described here.

Effect of Thapsigargin on the E2·BeF_3^- Crystal Structures. The crystal structures of E2·BeF_3^- with and without TG give us a number of clues to the mechanism of gating. As described, the structure in E2·BeF_3^-(−TG) is a composite of E1- and E2-type parts: the TGES loop, the M2 switch, and the position of the V-shaped structure are type E1; in contrast, the top part of M3, the inclination of the P-domain, and the positions of the M3–M4 helices are type E2. In the presence of TG, the A-domain rotates only ≈6°, but the M2 switch is changed to E2-like. As a result, the V-shaped structure is more inclined and farther down (SI Fig. 10). Accordingly the gate is fixed in the closed position. Then the question is whether the change in the M2 switch is made by such a small rotation of the A-domain. In other words, is the M2

switch fluctuating between the two types in solution, reflecting fluctuations in the A-domain position? The answer is perhaps yes.

Suzuki and colleagues (29, 30) beautifully demonstrated that a too-long A–M1′ link causes the accumulation of E2P·2Ca^{2+} (29) and a too-short one blocks E1P formation (30). In contrast, the mutants with too-long A–M1′ links can form E2P normally from Pi and hydrolyze it; furthermore, E2P·2Ca^{2+} can be formed from E2P and Ca^{2+} (29). These results indicate that, with the A-domain position realized in E2P, the TM structure can assume either an E1- or E2-type arrangement, when the restraint of the A–M1′ linker is removed. Their results also show that the restraint imposed by an A–M1′ linker at the correct length is necessary for reaching the second step of rotation, nicely corroborating the ideas presented here.

Methods

Crystallization. For E2·BeF_3^- crystals, affinity-purified enzyme (20 μM) in octaethyleneglycol mono-*n*-dodecylether ($C_{12}E_8$) and 1 mM Ca^{2+} was mixed with 3 mM EGTA, 8 mM NaF, 2 mM $BeCl_2$, and 10 mM $MgCl_2$ and then supplemented with 0.03 mM TG when desired; the specimen was dialyzed against a buffer consisting of 2.75 M glycerol, 10% PEG 1500, 10 mM $MgCl_2$, 2 mM $BeCl_2$, 8 mM NaF, 2.5 mM NaN_3, 2 μg/ml butylhydroxytoluene, 0.2 mM DTT, 1 mM EGTA, and 20 mM 3,3-dimethylglutaric acid (pH 5.7) at 10°C for up to 1.5 months. Before flash freezing, crystals were dialyzed against the crystallization buffer containing 14% PEG 1500, 8% sucrose, and 1% 2-methyl-2,4 pentanediol. E2·AlF_4^-(TG) crystals were prepared similarly, except that the enzyme was initially mixed with the solution containing 2 mM $AlCl_3$ and then dialyzed against a buffer consisting of 2.75 M glycerol, 8% PEG 2000, 1 mM $MgCl_2$, 2 mM $AlCl_3$, 8 mM NaF, 2.5 mM NaN_3, 2 μg/ml butylhydroxytoluene, 0.2 mM DTT, 1 mM EGTA, and 20 mM Mes (pH 6.1). E1·AlF_4^-·ADP crystals were prepared as before (8) but in the presence of 20 μM mastoparan and 2% (vol/vol) *t*-butanol.

Data Collection and Structure Determination. Crystals were picked with nylon loops in a cold room and, if necessary, left to stand for 2.5 min, after removing excess buffer for dehydration [only with E2·BeF_3^-(TG)] to improve the resolution. The packing was changed drastically by dehydration (SI Table 1). The crystals were then flash-frozen in cold nitrogen gas. Diffraction data were collected from crystals cooled to 100K at BL41XU of SPring-8 with an ADSC Q315 CCD detector. Structure was determined by molecular replacement using CNS (18). E2·BeF_3^-(−TG) was refined with restraints on hydrogen bonds (31). The atomic model of E1·AlF_4^-·ADP was refined with REFMAC including TLS refinement (32). Statistics of the diffraction data and refinement are given in SI Table 1.

We thank N. Shimizu and M. Kawamoto for data collection at BL41XU of SPring-8, Y. Kondou for structure refinement, J. Tsueda for technical assistance and making Fig. 7, D. B. McIntosh for help in improving the manuscript, and H. Suzuki and G. Inesi for providing information before publication and for stimulating discussions. This work is a part of an ongoing long-term project (2006B0013) at SPring-8. This work was supported in part by a Creative Science Project grant and Special Promoted Project grant from the Ministry of Education, Culture, Sports, Science and Technology of Japan.

1. MacLennan DH, Brandl CJ, Korczak B, Green NM (1985) *Nature* 316:696–700.
2. de Meis L, Vianna AL (1979) *Annu Rev Biochem* 48:275–292.
3. Albers RW (1967) *Annu Rev Biochem* 36:727–756.
4. Post RL, Hegyvary C, Kume S (1972) *J Biol Chem* 247:6530–6540.
5. Toyoshima C, Nakasako M, Nomura H, Ogawa H (2000) *Nature* 405:647–655.
6. Toyoshima C, Nomura H (2002) *Nature* 418:605–611.
7. Toyoshima C, Mizutani T (2004) *Nature* 430:529–535.
8. Toyoshima C, Nomura H, Tsuda T (2004) *Nature* 432:361–368.
9. Sørensen TL, Møller JV, Nissen P (2004) *Science* 304:1672–1675.
10. Olesen C, Sørensen TL, Nielsen RC, Møller JV, Nissen P (2004) *Science* 306:2251–2255.
11. Jensen AM, Sørensen TL, Olesen C, Møller JV, Nissen P (2006) *EMBO J* 25:2305–2314.
12. Toyoshima C, Inesi G (2004) *Annu Rev Biochem* 73:269–292.
13. Danko S, Yamasaki K, Daiho T, Suzuki H (2004) *J Biol Chem* 279:14991–14998.
14. Picard M, Toyoshima C, Champeil P (2006) *J Biol Chem* 281:3360–3369.
15. Moncoq K, Trieber CA, Young HS (2007) *J Biol Chem* 282:9748–9757.
16. Takahashi M, Kondou Y, Toyoshima C (2007) *Proc Natl Acad Sci USA* 104:5800–5805.
17. Danko S, Daiho T, Yamasaki K, Kamidochi M, Suzuki H, Toyoshima C (2001) *FEBS Lett* 489:277–282.
18. Brünger AT, Adams PD, Clore GM, DeLano WL, Gros P, Grosse-Kunstleve RW, Jiang JS, Kuszewski J, Nilges M, Pannu NS, *et al*. (1998) *Acta Crystallogr D* 54:905–921.
19. Wang W, Cho HS, Kim R, Jancarik J, Yokota H, Nguyen HH, Grigoriev IV, Wemmer DE, Kim SH (2002) *J Mol Biol* 319:421–431.
20. Troullier A, Girardet JL, Dupont Y (1992) *J Biol Chem* 267:22821–22829.
21. Hayward S (1999) *Proteins* 36:425–435.
22. Lewis RJ, Brannigan JA, Muchova K, Barak I, Wilkinson AJ (1999) *J Mol Biol* 294:9–15.
23. Clarke DM, Loo TW, MacLennan DH (1990) *J Biol Chem* 265:14088–14092.
24. Clausen JD, Vilsen B, McIntosh DB, Einholm AP, Andersen JP (2004) *Proc Natl Acad Sci USA* 101:2776–2781.
25. Ma H, Lewis D, Xu C, Inesi G, Toyoshima C (2005) *Biochemistry* 44:8090–8100.
26. Anthonisen AN, Clausen JD, Andersen JP (2006) *J Biol Chem* 281:31572–31582.
27. Yamasaki K, Daiho T, Danko S, Suzuki H (2004) *J Biol Chem* 279:2202–2210.
28. Møller JV, Lenoir G, Marchand C, Montigny C, le Maire M, Toyoshima C, Juul BS, Champeil P (2002) *J Biol Chem* 277:38647–38659.
29. Daiho T, Yamasaki K, Danko S, Suzuki H (2007) *J Biol Chem*, 10.1074/jbc.M707665200.
30. Daiho T, Yamasaki K, Wang G, Danko S, Iizuka H, Suzuki H (2003) *J Biol Chem* 278:39197–39204.
31. Fabiola F, Bertram R, Korostelev A, Chapman MS (2002) *Protein Sci* 11:1415–1423.
32. Winn MD, Isupov MN, Murshudov GN (2001) *Acta Crystallogr D* 57:122–133.
33. Kraulis PJ (1991) *J Appl Crystallogr* 24:946–950.
34. DeLano W (2002) The PyMOL Molecular Graphics System (DeLano Scientific, Palo Alto, CA).